Chiral bound states in the continuum: a higher-order singularity for on-chip control of quantum emission

Jin Li,[1] Kexun Wu,[1] Qi Hao,[2] Yan Chen,[3, *] and Jiawei Wang[1, †]

[1]*School of Integrated Circuits, Harbin Institute of Technology (Shenzhen), Shenzhen 518055, China*
[2]*Key Laboratory of Quantum Materials and Devices of Ministry of Education,*
School of Physics, Southeast University, Nanjing 210000, China
[3]*Institute for Quantum Science and Technology, National University of Defense Technology, Changsha 410073, China*
(Dated: October 28, 2025)

We demonstrate a fully integrable and reconfigurable platform for controlling quantum emission by harnessing chiral bound states in the continuum (BICs) as a higher-order non-Hermitian singularity. Our architecture employs dual-microring resonators evanescently coupled to two waveguides, supporting symmetry-protected BICs. By integrating an integrated reflector coupled with one resonator as a unidirectional feedback, a pair of orthogonal BICs gets transformed into a single, chiral BIC residing on an exceptional surface. The phase terms in external coupling and inter-modal coupling serve as two independent tuning knobs, enabling unprecedented dynamic control over the spontaneous emission dynamics of individual quantum emitters, including the Purcell enhancement and the emission lineshape. The efficiency in reconfiguring the output intensity gets promoted by more than a factor of two compared to alternative schemes, offering a promising path toward high-speed quantum optical switches and active lifetime control in integrated quantum photonic circuits.

In open physical systems, the intriguing features of non-Hermitian singularities shed profound light on light–matter interactions across classical and quantum domains [1–3]. Among these, a hallmark of such systems is the emergence of exceptional points (EPs), singularities where two or more eigenvalues and their corresponding eigenstates coalesce simultaneously, resulting in a collapse of the eigenspace's dimensionality [4, 5]. Furthermore, an equally captivating type of singularity in a non-Hermitian system is the "bound states in the continuum" (BICs) [6, 7], describing non-radiating resonances embedded within a continuum of radiating waves [8]. In recent explorations using optical microcavities, both of these peculiar singularities have been investigated for tailoring spontaneous emission in cavity quantum electrodynamics (cQED) systems [9–11], opening new pathways for the on-demand generation and manipulation of single photons as robust information carriers in quantum technologies [12–15].

Previous investigations of non-Hermitian cQED in solid-state platforms mainly employed conventional micro- and nanoresonator architectures [16–18], such as micropillars [19], circular Bragg gratings [20], photonic crystals [21–23], and Fabry-Perot cavities [24, 25], valued for their small mode volumes and high quality factors. Meanwhile, rapid progress in quantum photonic circuits is driving a shift toward integrated architectures. In this context, microring resonators arise as a promising alternative, offering not only inherent compatibility with on-chip, low-loss photonic elements [26], but also exceptional post-fabrication tunability, enabling dynamic reconfiguration of non-Hermitian parameters for quantum emission control [27–29]. A particularly elegant strategy for operating a microring system involves the integration of an external reflector, which deterministically couples one propagating mode (e.g., clockwise, CW) into its counter-propagating counterpart (counter-clockwise, CCW), thereby generating a chiral exceptional surface (ES) [11, 30–32]. Recently, such chiral ESs has been exploited to engineer spontaneous emission [33–35]. Despite these advances, tunability in key non-Hermitian parameters—particularly radiation through the continuum [28, 36, 37], remains largely unexplored in integrated cQED systems.

In this Letter, we demonstrate exquisite control of spontaneous emission from individual quantum emitters by engineering a chiral BIC in a dual-microring resonator system. By tailoring the phase accumulation within the bus waveguides coupled to two resonators, the radiation channels can be selectively enhanced or suppressed, ideally forming BICs. Concurrently, unidirectional mode coupling via an integrated reflector converts a pair of orthogonal BICs into a chiral one residing on an ES. While coupled to a single quantum emitter (QE), the system exploits two distinct non-Hermitian effects as independent knobs, enabling tunable enhancement of spontaneous emission and dynamic reshaping of its lineshape. Furthermore, for scalable quantum photonic circuits, efficient reconfiguration of both the Purcell factor and output intensity can be achieved with minimal phase tuning near a chiral quasi-BIC, thereby offering a promising route toward high-speed, on-chip quantum optical switches and active lifetime control of quantum emitters.

The discussion starts with a symmetric dual-microring resonator architecture, as illustrated in Fig. 1(a). Two microring resonators support two spectrally degenerate modes [4], namely, the CW and CCW propagating modes, and are not directly coupled. Instead, their interaction is mediated exclusively through two parallel bus waveguides. Since the out-coupled resonances in the two cavities through identical waveguides would interfere with each other, external coupling emerges as a critical
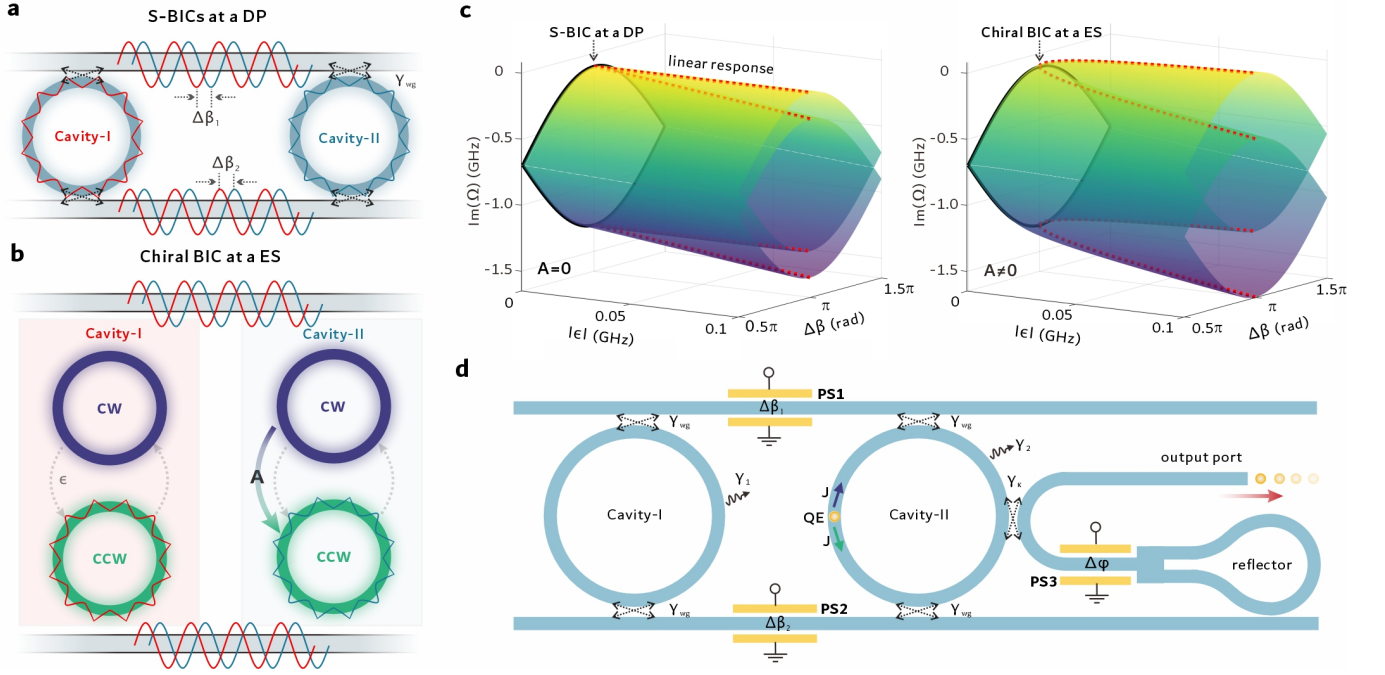
FIG. 1. (a) Schematic of S-BICs in a dual-ring resonator system. (b) Formation of a chiral BIC by introducing a unidirectional coupling term $\boldsymbol{A}$. (c) Numerically calculated imaginary parts of the eigenvalue surfaces in the $\varepsilon-\Delta\beta$ parameter space for the S-BIC (left) and chiral-BIC (right) systems. Here, we set $\gamma_1 = \gamma_2 + \gamma_\kappa = 0.2$ GHz, $\gamma_{\rm wg} = 0.4$ GHz, and $\Delta\omega = 0$. (d) Realization of a circuit-level cQED system harnessing a chiral quasi-BIC, including a QE embedded in cavity II and three phase shifters (PS1, PS2, and PS3). The QE couples to both CW and CCW modes with an identical electric dipole moment.

degree of freedom. By adopting a traveling-wave basis $[a_{\rm CCW}, a_{\rm CW}, b_{\rm CCW}, b_{\rm CW}]^{\rm T}$, where $\boldsymbol{a}$ and $\boldsymbol{b}$ correspond to the fields in the two cavities (see SM Note S1), the system can be described using the Hamiltonian as follows:

$$
H = \begin{pmatrix} \Omega_1 & 0 & \Gamma_1 & 0 \\ 0 & \Omega_1 & 0 & \Gamma_2 \\ \Gamma_2 & 0 & \Omega_2 & 0 \\ 0 & \Gamma_1 & 0 & \Omega_2 \end{pmatrix}, \tag{1}
$$

where $\Omega_1 = \omega_1 - i\gamma_1 - i2\gamma_{\rm wg}$, $\Omega_2 = \omega_2 - i\gamma_2 - i2\gamma_{\rm wg}$, $\Gamma_1 = -i2\gamma_{\rm wg}e^{i\Delta\beta_1}$, $\Gamma_2 = -i2\gamma_{\rm wg}e^{i\Delta\beta_2}$, ω_1 (ω_2) and γ_1 (γ_2) denote the resonance frequency and intrinsic cavity loss rate of the two cavities, respectively. $\gamma_{\rm wg}$ is the coupling rate between the resonators and the two bus waveguides, and $\Delta\beta_1$ ($\Delta\beta_2$) represent the relative phase shifts between the two interfering light waves for the two bus waveguides serving as radiation channels, respectively.

The phase terms between the two radiative components, $\Delta\beta_1$ and $\Delta\beta_2$, act as efficient parameters to regularize the external coupling. When the two resonances are degenerate and $\Delta\beta_1$ and $\Delta\beta_2$ are equal to $\pi/2$, the interference becomes maximally constructive, yielding predominant out-coupling through the waveguides. Conversely, when the phase shifts satisfy the destructive interference condition (i.e., $\Delta\beta_1 = \Delta\beta_2 = \pi$), the waveguide-induced leakage channels are eliminated, leading to a symmetry-protected bound state in the continuum (S-BIC) that exhibits an infinite radiative Q factor.

Notably, the normalized eigenvectors $[1, 0, 1, 0]^{\rm T}$ and $[0, 1, 0, 1]^{\rm T}$ reveal opposite mode chiralities and share a spectral degeneracy at a diabolic point (DP).

Here, by introducing a unidirectional coupling between the CW and CCW components (Fig. 1(b)), the original orthogonality between the pair of S-BICs gets broken. The system Hamiltonian is consequently modified to:

$$
H = \begin{pmatrix} \Omega_1 & 0 & \Gamma_1 & 0 \\ 0 & \Omega_1 & 0 & \Gamma_2 \\ \Gamma_2 & 0 & \Omega_2' & A \\ 0 & \Gamma_1 & 0 & \Omega_2' \end{pmatrix}, \tag{2}
$$

where $\Omega_2' = \omega_2 - i\gamma_2 - i\gamma_\kappa - i2\gamma_{\rm wg}$, $\boldsymbol{A}$ specifies the coupling coefficient (from the CW to the CCW mode in this case), and γ_κ accounts for the additional loss induced by the unidirectional coupling. Assuming a symmetric design of the two bus waveguides for simplicity (i.e., $\Delta\beta_1 = \Delta\beta_2 = \Delta\beta$), the eigenfrequencies and eigenvectors can be obtained as: $\Omega_\pm = \frac{\Omega_1 + \Omega_2'}{2} \pm \sqrt{\left(\frac{\Omega_1 - \Omega_2'}{2}\right)^2 + 4e^{i2\Delta\beta}\gamma_{\rm wg}^2}$, $v_\pm = \left(\frac{\Omega_1 - \Omega_2'}{2} \pm \sqrt{\left(\frac{\Omega_1 - \Omega_2'}{2}\right)^2 + 4e^{i2\Delta\beta}\gamma_{\rm wg}^2}, 0, 2e^{i\Delta\beta}\gamma_{\rm wg}, 0\right)^{\rm T}$.

The system's chirality becomes deterministic, with a purely CCW component existing. Here, different higher-order singularities can be engineered. A fourth-order EP can be reached by introducing $\Delta\omega = \omega_1 - \omega_2 = 2\gamma_{\rm wg}$

(see SM Note 2). For identical resonance frequencies ($\Delta\omega = 0$), a chiral quasi-BIC, as a peculiar type of higher-order singularity, can be established, featuring minimized radiation loss (limited by the presence of γ_κ).

In practice, fabrication imperfections (e.g., surface roughness) may randomly perturb the system and induce backscattering between the CW and CCW components. For simplicity, the perturbation Hamiltonian can be expressed as $H_{\text{perturb}} = \begin{pmatrix} \varepsilon & \varepsilon & 0 & 0 \\ \varepsilon & \varepsilon & 0 & 0 \\ 0 & 0 & \varepsilon & \varepsilon \\ 0 & 0 & \varepsilon & \varepsilon \end{pmatrix}$, where ε quantifies the perturbation strength applied uniformly to both microresonators.

Figure 1(c) summarizes the numerically calculated imaginary parts of the eigenvalue surfaces in the $|\varepsilon|$–$\Delta\beta$ parameter space for the two systems. For the conventional dual-ring system, when $|\varepsilon| = 0$, the radiation is regulated by $\Delta\beta$. The two curves correspond to the spectrally degenerate long- and short-lived modes, representing two DPs. As perturbations are introduced, four Riemann sheets reveal mode splitting with an amplitude linearly proportional to $|\varepsilon|$. In contrast, for the proposed system in Fig. 1(b), the two curves at $|\varepsilon| = 0$ essentially lie on the corresponding second-order ESs, where eigenvalues and eigenvectors coalesce simultaneously. Under perturbation, the eigenvalues exhibit a nonlinear enhancement proportional to $\sqrt{\varepsilon}$, directly reflecting the signature of an EP.

We now employ the peculiar chiral quasi-BIC shown in Fig. 1(b) for the regulation of on-chip integrated quantum sources. As illustrated in Fig. 1(d), a QE is located within the mode volume of cavity II. A waveguide integrated with a reflector (e.g., a Sagnac interferometer) provides the requisite non-Hermitian coupling, $\mathbf{A} = -2i\gamma_\kappa |r| \exp(-i\Delta\varphi)$, where r is the field reflection amplitude and $\Delta\varphi$ is the phase variation. The full Hamiltonian of this cQED system is detailed in SM Note S3. For semiconductor quantum dots with typical free-space lifetimes of $\sim$1–10 ns and integrated microrings offering photon lifetimes of $\sim$0.1–1 ns, the system operates in the weak-coupling regime [11, 35], where an emitted photon escapes before re-coupling to the emitter. Under this approximation, the dipole–cavity dynamics is governed by:

$$i\frac{d}{dt}\begin{pmatrix} a_{\text{CCW}} \\ a_{\text{CW}} \\ b_{\text{CCW}} \\ b_{\text{CW}} \end{pmatrix} = H \begin{pmatrix} a_{\text{CCW}} \\ a_{\text{CW}} \\ b_{\text{CCW}} \\ b_{\text{CW}} \end{pmatrix} + J \begin{pmatrix} 0 \\ 0 \\ e^{-i(\omega_{\text{QE}}t+\phi)} \\ e^{-i(\omega_{\text{QE}}t-\phi)} \end{pmatrix}, \quad (3)$$

where ω_{QE} is the emission frequency of the quantum emitter, J is the coupling constant for optical fields at a particular transverse position along the propagation direction for a traveling-wave resonance, and the phase term ϕ accounts for the accumulated dynamical phase between the emitter and a reference point (e.g., the waveguide–ring junction). The steady-state response can be obtained as: $\left(a_{CCW}, a_{CW}, b_{CCW}, b_{CW}\right)^T = G(\omega_{QE})\left(0, 0, Je^{-i\phi}, Je^{i\phi}\right)^T$, where $G(\omega_{\text{QE}}) = (\omega_{\text{QE}}I -$
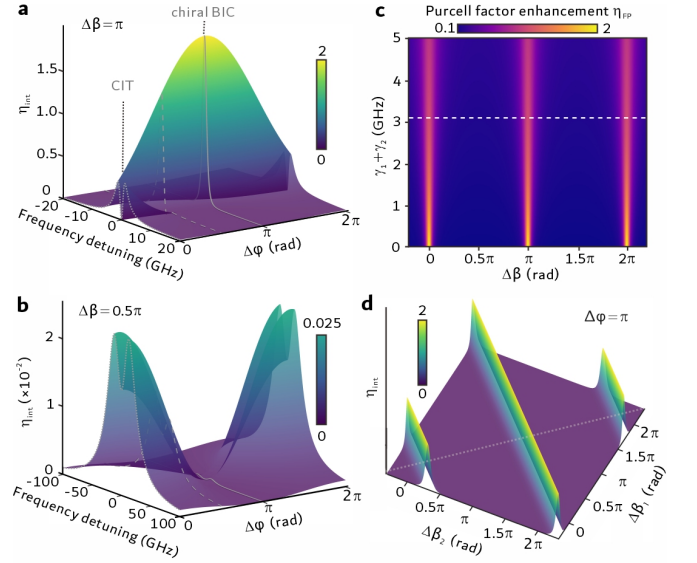

FIG. 2. (a–b) Calculated η_{int} versus frequency and phase difference $\Delta\varphi$ for $\Delta\beta = \pi$ (a) and $\Delta\beta = \pi/2$ (b). Here, we set $\Delta\omega = 0$, $\gamma_\kappa = 2.5$ GHz, $\gamma_{\text{wg}} = 5$ GHz, and $\gamma_1 = \gamma_2 = 0$ GHz. (c) Calculated η_{FP} as a function of $\Delta\beta$ and the sum of the intrinsic cavity losses, $\gamma_1 + \gamma_2$. The dashed line denotes the case for a typical TFLN-based microring resonator with an intrinsic Q factor of 20000. (d) Calculated η_{int} as a function of $\Delta\beta_1$ and $\Delta\beta_2$ at zero frequency detuning and $\Delta\varphi = \pi$. The dashed line denotes the ideal symmetric external coupling case where $\Delta\beta_1 = \Delta\beta_2$.

$H)^{-1}$ is the system's Green function (see SM Note S3) [38–40].

Here, we analyze the intensity collected at the remaining output port of the coupled waveguide (see Fig. 1(d)), which can be expressed as

$$I_{\text{output}} = \left| \sqrt{2\gamma_\kappa}\left(b_{\text{CW}}e^{i\Delta\varphi} + b_{\text{CCW}}\right) \right|^2, \quad (4)$$

where

$$b_{\text{CCW}} = \frac{-(\Omega_1 - \omega_{\text{QE}})Je^{i\phi}}{(\Omega_1 - \omega_{\text{QE}})(\Omega_2' - \omega_{\text{QE}}) - \Gamma_1\Gamma_2}$$
$$+ \frac{Je^{-i\phi}A(\Omega_1 - \omega_{\text{QE}})^2}{\left[(\Omega_1 - \omega_{\text{QE}})(\Omega_2' - \omega_{\text{QE}}) - \Gamma_1\Gamma_2\right]^2}, \quad (5)$$

$$b_{\text{CW}} = \frac{-(\Omega_1 - \omega_{\text{QE}})Je^{-i\phi}}{(\Omega_1 - \omega_{\text{QE}})(\Omega_2' - \omega_{\text{QE}}) - \Gamma_1\Gamma_2}. \quad (6)$$

For simplicity, the discussion adopts the approximation of negligible intrinsic backscattering ($\varepsilon = 0$, see discussions on the influence of backscattering in SM Note S4). Two phase terms, $\Delta\beta_1$ and $\Delta\beta_2$, are simultaneously tuned to an identical value $\Delta\beta$. To quantify the output spectral intensity at the port, we define a relative spontaneous emission intensity factor $\eta_{\text{int}} = \frac{I_{\text{output}}}{\max(I_{\text{DP}})}$, where I_{DP} is the total output intensity collected from a conventional waveguide-coupled microring within a cQED system (see SM Note S5). Figure 2(a) presents the evolution

of η_{int} when the system is configured to a chiral quasi-BIC ($\Delta\beta = \pi$). The emission lineshape is efficiently modified upon varying $\Delta\varphi$. The maximal intensity is obtained at $\Delta\varphi = \pi$, exhibiting a squared-Lorentzian profile in sharp contrast to the regular Lorentzian profile in the conventional DP case. At $\Delta\varphi = 0$, the resulting spectrum is doublet-shaped with a zero value at the central frequency. This "chirality-induced transparency (CIT)" phenomenon arises from perfect destructive interference between the CCW and back-reflected components. When the system is tuned away from the chiral quasi-BIC ($\Delta\beta = \pi/2$, Fig. 2(b)), the reinforced external coupling via the two bus waveguides as the continuum does not lead to a homogeneous suppression of the spectra upon varying $\Delta\varphi$. Instead, the minimal emission intensity is reached at $\Delta\varphi = \pi$, which is only $\sim 0.01\%$ of the maximized value in Fig. 2(a).

To quantitatively elucidate the cavity enhancement within the weak coupling regime, the local density of optical states and the Purcell enhancement factor can be expressed as [9, 10, 40]:

$$\rho_{\mathrm{LDOS}}(\omega_{\mathrm{QE}}) = -\frac{2}{\hbar\varepsilon_0}\mathbf{d}\,\mathrm{Im}\left[G(\omega_{\mathrm{QE}})\right]\mathbf{d}^*, \qquad (7)$$

$$F_p(\omega_{\mathrm{QE}}) = 1 + \frac{\rho_{\mathrm{LDOS}}(\omega_{\mathrm{QE}})}{\rho_{\mathrm{hom}}}, \qquad (8)$$

where $\mathbf{d}$ denotes the dipole moment vector of the QE (in this case, $\mathbf{d} = [0, 0, 1, 1]^{\mathrm{T}}$), and ρ_{hom} represents the LDOS in a homogeneous medium. Here we introduce an enhancement factor of the Purcell factor, η_{FP}, defined as $\eta_{\mathrm{FP}} = \frac{F_P(\omega_{\mathrm{QE}})}{F_{P,\mathrm{DP}}(\omega_{\mathrm{QE}})}$, where $F_{P,\mathrm{DP}}$ denotes the Purcell factor under the DP condition.

Figure 2(c) presents the calculated η_{FP} as a function of $\Delta\beta$ and the total intrinsic cavity losses, $\gamma_1 + \gamma_2$. η_{FP} reaches a maximum of 2 at an optimally configured chiral quasi-BIC and decreases as the system moves away from this singularity. The upper bound of η_{FP} is fundamentally constrained by the intrinsic cavity losses. The experimental configuration, featuring two integrated phase shifters for the independent control of $\Delta\beta_1$ and $\Delta\beta_2$, enables dynamic reconfiguration of the emission dynamics. As revealed in Fig. 2(d), by keeping one phase constant, both the output intensity and F_P can be efficiently tuned while preserving near-optimal enhancement close to the chiral quasi-BIC (see SM Note S6 for details). This flexibility underscores the potential for on-chip reconfiguration of quantum emission dynamics.

Beyond the analytical model, we further investigate a practical chiral BIC on a thin-film lithium niobate (TFLN) integrated photonic platform, notable for hybrid integration with semiconductor quantum dots as an on-chip quantum source [31, 41]. Two-dimensional finite-element simulations (COMSOL) are performed. As shown in Fig. 3(a), the squared-Lorentzian lineshape at $\Delta\beta = \pi$ and the mode-splitting doublet feature at $\Delta\beta = \pi/2$ are obtained, producing a colossal intensity
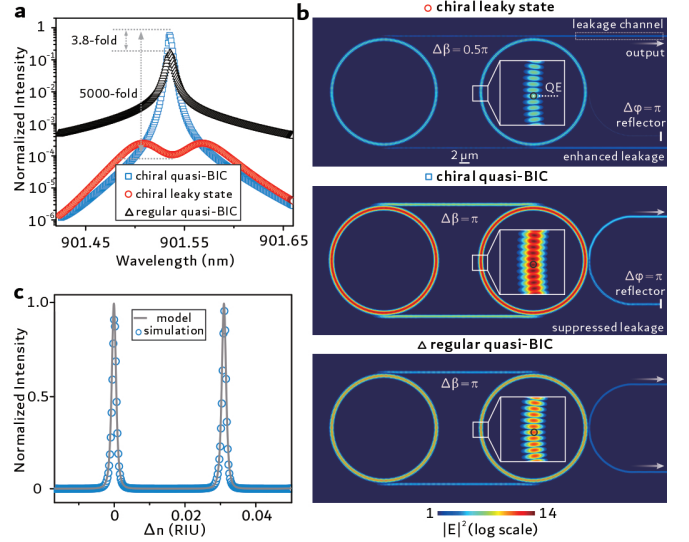

FIG. 3. (a) Simulated output spectra for the chiral quasi-BIC ($\Delta\varphi = \pi$, $\Delta\beta = \pi$), chiral leaky state ($\Delta\varphi = \pi$, $\Delta\beta = \pi/2$), and regular quasi-BIC ($\Delta\beta = \pi$). Simulations use a refractive index contrast of $2/1.55$ between LN waveguides and silica cladding. The two identical microrings have a radius of 10 μm, bus waveguides and rings are 400 nm wide with a 250 nm coupling gap. The feedback waveguide has a 300 nm gap and a perfect electric conductor at its end as a reflector. The QE is modeled as a point dipole mimicking a hybrid InGaAs quantum dot at ~ 901 nm. (b) Mode electric field intensity $|E|^2$ on a logarithmic scale for the three cases in (a). Insets: zoomed-in views of the region surrounding the embedded QE. (c) Extracted output normalized intensity versus Δn applied to the bus waveguides. Solid line: theoretical fit.

contrast of 5000-fold through phase tuning. The distinct external coupling behaviors are further ascertained by the simulated mode field profiles in Fig. 3(b) (top and middle panels). In comparison, the regular dual-ring system (Fig. 3(b), bottom) demonstrates that the regular quasi-BIC exhibits a 3.8-fold reduction in output intensity relative to the chiral quasi-BIC (see SM Note S7 for details). By locally tuning the refractive index of the two bus waveguides via integrated phase shifters (Fig. 3(c)), the output spectral intensity can be fully adjusted between 10^{-4} and 1, with the modulation curve closely matching the theoretical model in Fig. 2(d).

Both theory and simulations show that operating near a chiral quasi-BIC enables efficient reconfiguration of spontaneous emission. Here, we compare η_{int} reconfiguration with two previously explored schemes. In a conventional microring-resonator-based cQED system, reconfiguration can be performed via resonance detuning between the resonant mode and ω_{QE}. Considering practical intrinsic cavity losses of ~ 15 GHz (corresponding to an intrinsic Q factor of 20000 [41]), a 20 dB dynamic range in η_{int} requires a phase tuning amplitude of $\sim 0.5\pi$ (Fig. 4(a) top). Notably, by engineering the resonant mode from a common DP to a chiral EP, the maximal η_{int} is enhanced by two-fold (Fig. 4(a) middle). An equiv-
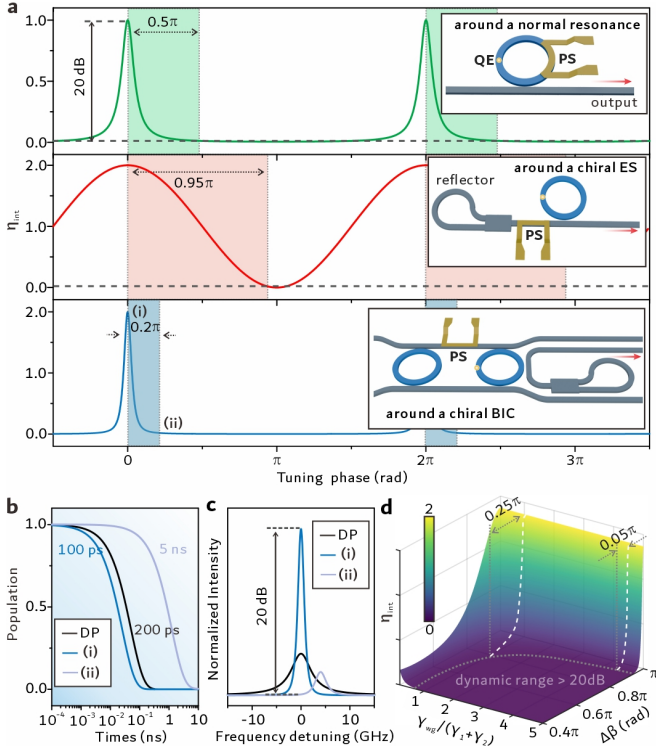
FIG. 4. (a) Calculated η_{int} versus applied phase for three different configurations, including the conventional microring system operated at a DP (top), the single microring system operated at a chiral ES (middle), and a dual-ring system operated around a chiral quasi-BIC (bottom). Insets: corresponding system schematics. (b) Calculated lifetime traces of a single QE upon reconfiguration of $\Delta\beta$. (c) Calculated emission spectra upon reconfiguration of $\Delta\beta$. The cases under a DP condition are also presented in (b–c) for comparison. (d) Map of η_{int} as a function of $\Delta\beta$ and the loss contrast $\gamma_{\text{wg}}/(\gamma_1 + \gamma_2)$. The dashed lines indicate the phase amplitude required for a 20 dB dynamic range of η_{int}.

diation rate corresponds to distinct emission lineshapes in the spectral domain (Fig. 4(c)).

This stands in stark contrast to conventional paradigms, where the radiation loss remains static. Our approach transcends this limitation by leveraging multiple degrees of freedom to reconfigure the non-Hermiticity around the chiral quasi-BIC. Both phase shifters on the two bus waveguides can be utilized with an equal amount of tuning, resulting in a doubling of tuning efficiency. Furthermore, the external coupling loss γ_{wg} can be readily adjusted by changing the gap spacing between the bus waveguides and microrings. Figure 4(d) presents the mapping of η_{int} upon the regulation of the loss ratio between the external coupling and intrinsic cavity, $\gamma_{\text{wg}}/(\gamma_1 + \gamma_2)$, and $\Delta\beta$. The mapping reveals that the phase tuning required to achieve a 20 dB dynamic range can be drastically reduced to one-quarter of its original value by simply increasing γ_{wg} by a factor of 4.5.

In summary, we have theoretically demonstrated an integrated cQED system combining two non-Hermitian singularities to achieve precise control over quantum light emission. The introduced chiral BIC features maximal mode chirality at an EP and meanwhile ideally zero radiation loss. By reconfiguring the system around such a higher-order singularity, the spontaneous emission dynamics, including the emission intensity, lifetime, and spectra lineshape, can be freely manipulated with minimized requirement of phase tuning amplitude in the external coupling. Looking forward, this concept is well-suited for various material platforms with integrated QEs, especially TFLN [27, 29, 31], silicon nitride, and silicon carbide. The demonstrated on-the-fly reconfigurability positions this device as a versatile building block that can be dynamically configured as either an on-chip single-photon source, quantum optical switch, or long-lived quantum memory [42], which is a critical capability for scalable quantum computing [26] and communicating architectures.

alent dynamic reconfiguration can now be achieved by steering the system towards the vicinity of CIT, requiring phase tuning of $\Delta\varphi \sim 0.95\pi$ on the feedback arm of the reflector.

Strikingly, in our proposed system, the maximal η_{int} matches that of the chiral EP scheme. In contrast, the reconfiguration is accomplished by varying the external coupling strength. A 20 dB dynamic range requires tuning one of the two external coupling channels (i.e., $\Delta\beta_1$ or $\Delta\beta_2$) to $\sim 0.2\pi$ (Fig. 4(a) bottom). Assuming a radiative lifetime of 200 ps in a DP condition as a baseline, such tuning facilitates reconfiguration of the lifetime between 100 ps and 5 ns (Fig. 4(b)). Moreover, the regulated ra-

* chenyan@nudt.edu.cn
† wangjw7@hit.edu.cn

[1] M. A. Miri and A. Alu, Exceptional points in optics and photonics, Science 363, aar7709 (2019).

[2] S. K. Ozdemir, S. Rotter, F. Nori, and L. Yang, Parity-time symmetry and exceptional points in photonics, Nat. Mater. **18**, 783 (2019).

[3] C. Wang, Z. Fu, W. Mao, J. Qie, A. D. Stone, and L. Yang, Non-Hermitian optics and photonics: from classical to quantum, Adv. Opt. Photon. **15**, 442 (2023).

[4] H. Cao and J. Wiersig, Dielectric microcavities: Model systems for wave chaos and non-Hermitian physics, Rev. Mod. Phys. **87**, 61 (2015).

[5] K. Ding, C. Fang, and G. Ma, Non-Hermitian topology and exceptional-point geometries, Nat. Rev. Phys. **4**, 745 (2022).

[6] M. Kang, T. Liu, C. T. Chan, and M. Xiao, Applications of bound states in the continuum in photonics, Nat. Rev. Phys. **5**, 659 (2023).

[7] D. C. Marinica, A. G. Borisov, and S. V. Shabanov, Bound states in the continuum in photonics, Phys. Rev. Lett. **100**, 183902 (2008).

[8] C. W. Hsu, B. Zhen, A. D. Stone, J. D. Joannopoulos, and M. Soljačić, Bound states in the continuum, Nat. Rev. Mater. **1**, 16048 (2016).

[9] L. Ferrier, P. Bouteyre, A. Pick, S. Cueff, N. H. M. Dang, C. Diederichs, A. Belarouci, T. Benyattou, J. X. Zhao, R. Su, J. Xing, Q. Xiong, and H. S. Nguyen, Unveiling the enhancement of spontaneous emission at exceptional points, Phys. Rev. Lett. **129**, 083602 (2022).

[10] P. Lodahl, S. Mahmoodian, and S. Stobbe, Interfacing single photons and single quantum dots with photonic nanostructures, Rev. Mod. Phys. **87**, 347 (2015).

[11] Q. Zhong, A. Hashemi, c. K. özdemir, and R. El-Ganainy, Control of spontaneous emission dynamics in microcavities with chiral exceptional surfaces, Phys. Rev. Res. **3**, 013220 (2021).

[12] T. T. H. Do, M. Nonahal, C. Li, V. Valuckas, H. H. Tan, A. I. Kuznetsov, H. S. Nguyen, I. Aharonovich, and S. T. Ha, Room-temperature strong coupling in a single-photon emitter-metasurface system, Nat. Commun. **15**, 2281 (2024).

[13] L. Leonforte, A. Carollo, and F. Ciccarello, Vacancy-like dressed states in topological waveguide QED, Phys. Rev. Lett. **126**, 063601 (2021).

[14] Y.-W. Lu, W. Li, and X.-H. Wang, Quantum and classical exceptional points at the nanoscale: Properties and applications, ACS Nano **19**, 17953 (2025).

[15] Y. Sato, Y. Tanaka, J. Upham, Y. Takahashi, T. Asano, and S. Noda, Strong coupling between distant photonic nanocavities and its dynamic control, Nat. Photon. **6**, 56 (2012).

[16] I. Aharonovich, D. Englund, and M. Toth, Solid-state single-photon emitters, Nat. Photon. **10**, 631 (2016).

[17] F. P. García de Arquer, D. V. Talapin, V. I. Klimov, Y. Arakawa, M. Bayer, and E. H. Sargent, Semiconductor quantum dots: Technological progress and future challenges, Science **373**, eaaz8541 (2021).

[18] Z. Qian, L. Shan, X. Zhang, Q. Liu, Y. Ma, Q. Gong, and Y. Gu, Spontaneous emission in micro- or nanophotonic structures, PhotoniX **2**, 21 (2021).

[19] M. Lermer, N. Gregersen, F. Dunzer, S. Reitzenstein, S. Höfling, J. Mørk, L. Worschech, M. Kamp, and A. Forchel, Bloch-wave engineering of quantum dot micropillars for cavity quantum electrodynamics experiments, Phys. Rev. Lett. **108**, 057402 (2012).

[20] B. Lefaucher, J.-B. Jager, V. Calvo, F. Cache, A. Durand, V. Jacques, I. Robert-Philip, G. Cassabois, Y. Baron, F. Mazen, S. Kerdilès, S. Reboh, A. Dréau, and J.-M. Gérard, Purcell enhancement of silicon w centers in circular bragg grating cavities, ACS Photonics **11**, 24 (2024).

[21] D. Englund, D. Fattal, E. Waks, G. Solomon, B. Zhang, T. Nakaoka, Y. Arakawa, Y. Yamamoto, and J. Vučković, Controlling the spontaneous emission rate of single quantum dots in a two-dimensional photonic crystal, Phys. Rev. Lett. **95**, 013904 (2005).

[22] Y.-T. Wang, Q.-H. Ye, J.-Y. Yan, Y. Qiao, Y.-X. Liu, Y.-Z. Ye, C. Chen, X.-T. Cheng, C.-H. Li, Z.-J. Zhang, C.-N. Huang, Y. Meng, K. Zou, W.-K. Zhan, C. Zhao, X. Hu, C. A. T. H. Tee, W. E. I. Sha, Z. Huang, H. Liu, C.-Y. Jin, L. Ying, and F. Liu, Moiré cavity quantum electrodynamics, Sci. Adv. **11**, eadv8115 (2025).

[23] S. Yan, H. Li, J. Yang, X. Chen, H. Liu, D. Dai, R. Zhu, Z. Ma, S. Shi, L. Yang, Y. Yuan, W. Dai, D. Dai, B. Fu, Z. Zuo, H. Ni, Z. Niu, C. Wang, K. Jin, Q. Gong, and X. Xu, Cavity quantum electrodynamics with moiré photonic crystal nanocavity, Nat. Commun. **16**, 4634 (2025).

[24] S. Haroche, M. Brune, and J. M. Raimond, From cavity to circuit quantum electrodynamics, Nat. Phys. **16**, 243 (2020).

[25] S. Liu, C. Gustin, H. Liu, X. Li, Y. Yu, H. Ni, Z. Niu, S. Hughes, X. Wang, and J. Liu, Dynamic resonance fluorescence in solid-state cavity quantum electrodynamics, Nat. Photon. **18**, 318 (2024).

[26] E. Pelucchi, G. Fagas, I. Aharonovich, D. Englund, E. Figueroa, Q. Gong, H. Hannes, J. Liu, C.-Y. Lu, N. Matsuda, J.-W. Pan, F. Schreck, F. Sciarrino, C. Silberhorn, J. Wang, and K. D. Jöns, The potential and global outlook of integrated photonics for quantum technologies, Nat. Rev. Phys. **4**, 194 (2022).

[27] M. Davanco, J. Liu, L. Sapienza, C.-Z. Zhang, J. V. De Miranda Cardoso, V. Verma, R. Mirin, S. W. Nam, L. Liu, and K. Srinivasan, Heterogeneous integration for on-chip quantum photonic circuits with single quantum dot devices, Nat. Commun. **8**, 889 (2017).

[28] J. Li, M. Tang, X. Wang, C. N. Saggau, Y. Yin, L. Ma, Q. Song, O. G. Schmidt, and J. Wang, Reconfigurable resonance trapping in single optical microresonators, Newton **1**, 100171 (2025).

[29] Y. Zhu, R. Liu, A. Yi, X. Wang, Y. Qin, Z. Zhao, J. Zhao, B. Chen, X. Zhang, S. Song, Y. Huo, X. Ou, and J. Zhang, A hybrid single quantum dot coupled cavity on a CMOS-compatible sic photonic chip for Purcell-enhanced deterministic single-photon emission, Light Sci. Appl. **14**, 86 (2025).

[30] H.-Z. Chen, T. Liu, H.-Y. Luan, R.-J. Liu, X.-Y. Wang, X.-F. Zhu, Y.-B. Li, Z.-M. Gu, S.-J. Liang, H. Gao, L. Lu, L. Ge, S. Zhang, J. Zhu, and R.-M. Ma, Revealing the missing dimension at an exceptional point, Nat. Phys. **16**, 571 (2020).

[31] Y. Chen, X. Wang, J. Li, R. Su, K. Xiong, X. Li, Y. Yu, T. Zhang, K. Wu, X. Li, J. Wang, J. Zhang, J. Liu, and T. Jiang, On-chip non-Hermitian cavity quantum electrodynamics (2025), arXiv:2505.05490 [physics.optics].

[32] Q. Zhong, J. Ren, M. Khajavikhan, D. N. Christodoulides, S. K. Ozdemir, and R. El-Ganainy, Sensing with exceptional surfaces in order to combine sensitivity with robustness, Phys. Rev. Lett. **122**, 153902 (2019).

[33] K. Liao, Y. Zhong, Z. Du, G. Liu, C. Li, X. Wu, C. Deng, C. Lu, X. Wang, C. T. Chan, Q. Song, S. Wang, X. Liu,

X. Hu, and Q. Gong, On-chip integrated exceptional surface microlaser, Sci. Adv. **9**, eadf3470 (2023).

[34] Y.-W. Lu, J.-F. Liu, R. Liu, and H.-X. Jiang, Enhanced quantum coherence of plasmonic resonances with a chiral exceptional points, Commun. Phys. **7**, 166 (2024).

[35] Y. Lu, Y. Zhao, R. Li, and J. Liu, Anomalous spontaneous emission dynamics at chiral exceptional points, Opt. Express **30**, 473824 (2022).

[36] A. Canós Valero, Z. Sztranyovszky, E. A. Muljarov, A. Bogdanov, and T. Weiss, Exceptional bound states in the continuum, Phys. Rev. Lett. **134**, 103802 (2025).

[37] M. Pelton, Modified spontaneous emission in nanophotonic structures, Nat. Photon. **9**, 427 (2015).

[38] S. Franke, J. Ren, M. Richter, A. Knorr, and S. Hughes, Fermi's golden rule for spontaneous emission in absorptive and amplifying media, Phys. Rev. Lett. **127**, 013602 (2021).

[39] A. Hashemi, K. Busch, D. N. Christodoulides, S. K. Ozdemir, and R. El-Ganainy, Linear response theory of open systems with exceptional points, Nat. Commun. **13**, 3281 (2022).

[40] J. Ren, S. Franke, and S. Hughes, Quasinormal modes, local density of states, and classical Purcell factors for coupled loss-gain resonators, Phys. Rev. X **11**, 041020 (2021).

[41] X. Wang, Y. Zhu, X. Zhang, Y. Qin, B. Chen, Y. Chen, Y. Huo, J. Zhang, and X. Ou, Hybrid and scalable photonic circuit cavity quantum electrodynamics (2025), arXiv:2504.04671 [quant-ph].

[42] Y.-P. Liu, Z.-W. Ou, T.-X. Zhu, M.-X. Su, C. Liu, Y.-J. Han, Z.-Q. Zhou, C.-F. Li, and G.-C. Guo, A millisecond integrated quantum memory for photonic qubits, Sci. Adv. **11**, eadu5264 (2025).